Draft version September 9, 2023
Typeset using LATEX twocolumn style in AASTeX631

Feeding the Central Molecular Zone

Andy Nilipour,[1,2] Juergen Ott,[2] David Meier,[3,2] and Brian Svoboda[2]

[1]Department of Astronomy, Yale University, Steinbach Hall, 52 Hillhouse Ave, New Haven, CT 06511
[2]National Radio Astronomy Observatory, PO Box O, 1003 Lopezville Road, Socorro, NM 87801
[3]New Mexico Institute of Mining and Technology, 801 Leroy Place, Socorro, NM 87801

ABSTRACT

The Central Molecular Zone (CMZ) of the Milky Way is fed by gas inflows from the Galactic disk, but despite being fundamental to all processes in the inner Milky Way, these inflows are much less well-understood than the CMZ itself. We observed 25 clouds in the Galactic disk with $|\ell| < 10°$ which are candidates for gas accreting onto the CMZ due to their warm temperatures and broad lines. We present observations of the SiO $J = 5 \rightarrow 4$, H_2CO $J = 3_{21} \rightarrow 2_{20}$, H_2CO $J = 3_{03} \rightarrow 2_{02}$, HC_3N $J = 24 \rightarrow 23$, CH_3OH $J = 4_{22} \rightarrow 3_{12}$, $C^{18}O$ $J = 2 \rightarrow 1$, ^{13}CO $J = 2 \rightarrow 1$, ^{12}CO $J = 2 \rightarrow 1$, and H30α spectral lines with the Atacama Large Millimeter/submillimeter Array (ALMA) Atacama Compact Array (ACA). We measure temperatures, shocks, star formation rates, and turbulent Mach numbers for all of these clouds, providing a grid of cloud properties within the inner Galaxy. We find that although the clouds likely do not lie along the CMZ inflows, there are several clouds associated with regions that may be undergoing high velocity collisions. We also look into the differences in properties and kinematics probed by the ammonia and formaldehyde thermometers.

1. INTRODUCTION

The Central Molecular Zone (CMZ) is a region of molecular gas at high density and pressure within the inner ∼250 pc of the Milky Way. The CMZ is contained within the Galactic bar, which has a radius of about 5 kpc (Bland-Hawthorn & Gerhard 2016). A non-axisymmetric bar potential allows for two primary closed orbits, the x_1 and x_2 orbits (Contopoulos & Grosbøl 1989). x_1 orbits are elongated parallel to the major axis of the bar and can form cusps and self-intersecting loops, whereas x_2 are closer to the Galactic center and are elongated parallel to the minor axis of the bar. Shocks that are formed at the self-intersections of material on x_1 orbits drive gas to x_2 orbits (Binney et al. 1991). This material on x_2 orbits comprises the CMZ (Sormani et al. 2015), and the gas transitioning from x_1 to x_2 orbits are believed to form bar lanes that feed the CMZ.

While the CMZ has been extensively studied at many wavelengths (eg. Kruijssen et al. 2014; Jones et al. 2012; Ginsburg et al. 2016; Oka et al. 2005), the bar lanes and inflows have been relatively neglected. Sormani & Barnes (2019) calculated the gas inflow rate to be $2.7^{+1.5}_{-1.7}$ $M_\odot$ yr^{-1} using previous observations of ^{12}CO and a simple geometrical model of the inner Galaxy, but simulations show more complex dynamics, such as inflowing gas overshooting the CMZ and subsequently colliding with the bar lane on the opposite side (Sormani et al. 2019), which reduces the CMZ gas accretion rate to 0.8 ± 0.6 $M_\odot$ yr^{-1} (Hatchfield et al. 2021). It has been suggested that clouds such as Bania 2 (B2; Stark & Bania 1986) and G5, which have broad lines, warm temperatures, and shocked gas, are sites of cloud-cloud collisions along the bar lanes (Sormani & Barnes 2019, Gramze et al *in press*).

As gas flows along the bar lanes toward the CMZ, it is believed to undergo many processes that inhibit star formation (Krumholz et al. 2017), but observations of such processes have been limited. However, studying the properties and dynamics of these gas flows is essential to understanding the inner galaxy as a whole. In this paper, we have selected 25 clouds in the Galactic bar region, including several located within B2 and G5 and excluding the CMZ, that show bright NH_3 (3,3) emission in the Mopra HOPS survey (Walsh et al. 2011; Purcell et al. 2012; Longmore et al. 2017) and that have broad lines ($\gtrsim$ 10 km/s) and gas temperatures warmer than typical clouds in the Galactic disk ($\gtrsim$ 10-20 K). We use the Atacama Large Millimeter/submillimeter Array (ALMA) Atacama Compact Array (ACA) to observe several molecular lines from these 25 clouds in order to probe physical parameters including temperature, shocks, ionization, star formation, and turbulence, and to investigate whether these clouds are comprised of molecular gas that is feeding or that has overshot the CMZ. In Section 2 we describe the observations, ancillary data, and data reduction procedure. In Section 3 we calculate and compare the temperature, turbulence, and star forming properties of the clouds. In Section 4 we look into the shock properties of the clouds. In Section 5 we discuss the locations of the clouds and the relationships between their properties, and we conclude in Section 6.

2. OBSERVATIONS AND DATA REDUCTION

2.1. *ALMA Observations and Data Reduction*

The spatial distribution of the 25 selected clouds are shown in Figure 1. Using a Galactic Center distance of 8178 ± 26 pc (Abuter et al. 2019) and an angle between the Galactic bar and the line-of-sight of $30° \pm 2°$ (Wegg et al. 2015), we can calculate the distance and Galactocentric radius of each cloud. We also include a 1 kpc uncertainty along the line-of-sight to account for finite bar thickness. The locations of each cloud are detailed in Table 1. However, we note in Section 5 that it is likely that many of the clouds in our sample are not located on the bar, and so the Galactocentric radii and distances may be inaccurate for the individual clouds.

The clouds were observed with the ALMA ACA between May 2021 and May 2023 (project codes: 2019.2.00068.S, 2021.2.00001.S, 2022.1.00591.S; PI: Ott, J.) using both the 7m array and the Total Power (TP) antennas. We focus primarily on the TP data in this work. The spectral windows used cover several important spectral lines: the carbon monoxide isotopologues ^{12}CO $J = 2 \rightarrow 1$, ^{13}CO $J = 2 \rightarrow 1$, and C^{18}CO $J = 2 \rightarrow 1$; the shock tracers SiO $J = 5 \rightarrow 4$ (Schilke et al. 1997) and CH_3OH $J = 4_{22} \rightarrow 3_{12}$ (Meier & Turner 2005); the formaldehyde lines H_2CO $J = 3_{03} \rightarrow 2_{02}$ and H_2CO $J = 3_{22} \rightarrow 2_{21}$; the dense molecular gas tracer HC_3N $J = 24 \rightarrow 23$ (Mills et al. 2018); and the radio recombination line H(30)α. The observing parameters of the spectral windows are shown in Table 2.

We used the default ALMA Pipeline Reduction, which utilized the Common Astronomy Software Application (CASA) versions 6.2.1.7-6.4.1.12 (The CASA Team et al. 2022). We received 8 TP spectral cubes per cloud, for a total of 200. Some of the TP data was processed with the Single Dish Pipeline version 2022.2.0.64, which was affected with an issue causing spurious dark and bright spots in the data cubes; these were later reprocessed and found to fulfill the quality assurance standards. We recorded the velocity and channel ranges without any spectral features and those covering the target cloud for each cube.

The native FWHM beam size of the observations are between approximately 28" and 30". We smooth the cubes to all have the same beam size of 31". For each cloud, we also regrid the cubes to match the ^{13}CO $J = 2 \rightarrow 1$ pixel size and velocity resolution, resulting in a pixel size of 2.935" and a velocity resolution of 0.332 km s^{-1}. We then convert from intensity I_ν in units of Jy beam^{-1} to a brightness temperature using the equation

$$T_B = 1.222 \times 10^6 \left(\frac{I_\nu}{\text{Jy beam}^{-1}}\right)\left(\frac{\text{GHz}}{\nu^2}\right)^2\left(\frac{\text{"} \times \text{"}}{\theta_{\min}\theta_{\text{maj}}}\right) \quad (1)$$

where ν is the line rest frequency and $\theta_{\text{maj}} = \theta_{\min} = 31$" are the FWHM beam size along the major and minor axes of our smoothed data. To remove baselines, we also subtract a linear fit to the line-free channels.

Cloud	ℓ	b	R_{Gal} [kpc]	D [kpc]
1	8.68	-0.37	1.97 ± 0.09	6.54 ± 1.04
2	8.41	-0.29	1.92 ± 0.08	6.58 ± 1.04
3	6.91	-0.23	1.64 ± 0.08	6.81 ± 1.05
4	6.56	-0.30	1.57 ± 0.07	6.86 ± 1.05
6	5.75	0.23	1.40 ± 0.07	7.00 ± 1.06
7	5.49	-0.08	1.35 ± 0.07	7.04 ± 1.06
8	5.38	-0.12	1.32 ± 0.07	7.06 ± 1.06
10	3.43	-0.35	0.89 ± 0.05	7.42 ± 1.07
13	3.09	0.16	0.81 ± 0.04	7.49 ± 1.08
14	3.02	-0.07	0.79 ± 0.04	7.50 ± 1.08
15	2.96	-0.19	0.78 ± 0.04	7.52 ± 1.08
17	2.51	-0.03	0.67 ± 0.04	7.61 ± 1.08
18	1.93	0.11	0.52 ± 0.03	7.73 ± 1.09
19	358.48	-0.38	0.45 ± 0.03	8.57 ± 1.14
20	354.60	0.47	1.85 ± 0.14	9.82 ± 1.25
21	353.42	-0.36	2.36 ± 0.19	10.29 ± 1.30
22	351.79	-0.49	3.15 ± 0.27	11.02 ± 1.39
23	351.58	-0.34	3.25 ± 0.29	11.12 ± 1.40
24	350.18	0.02	4.04 ± 0.38	11.85 ± 1.51
25	350.11	0.09	4.09 ± 0.39	11.89 ± 1.51

Table 1. Locations of all clouds.

2.2. *ALMA Maps*

To make moment 0 (integrated intensity) maps, we set a cutoff at $4\sigma_{\text{rms}}$, where we take σ_{rms} to be the root-mean-square noise (rms) over the line-free channels, then integrate over the velocity range of the cloud in ^{13}CO $J = 2 \rightarrow 1$, which is observed for all clouds and is less contaminated than the more common isotopologue ^{12}CO $J = 2 \rightarrow 1$. We also generated moment 1 (intensity weighted velocity), moment 2 (velocity dispersion), and moment 8 (peak intensity) maps from each cube using a 5σ cutoff on the moment 0 map. We estimate

$$\sigma \approx \sqrt{N}\sigma_{\text{rms}}\Delta v \quad (2)$$

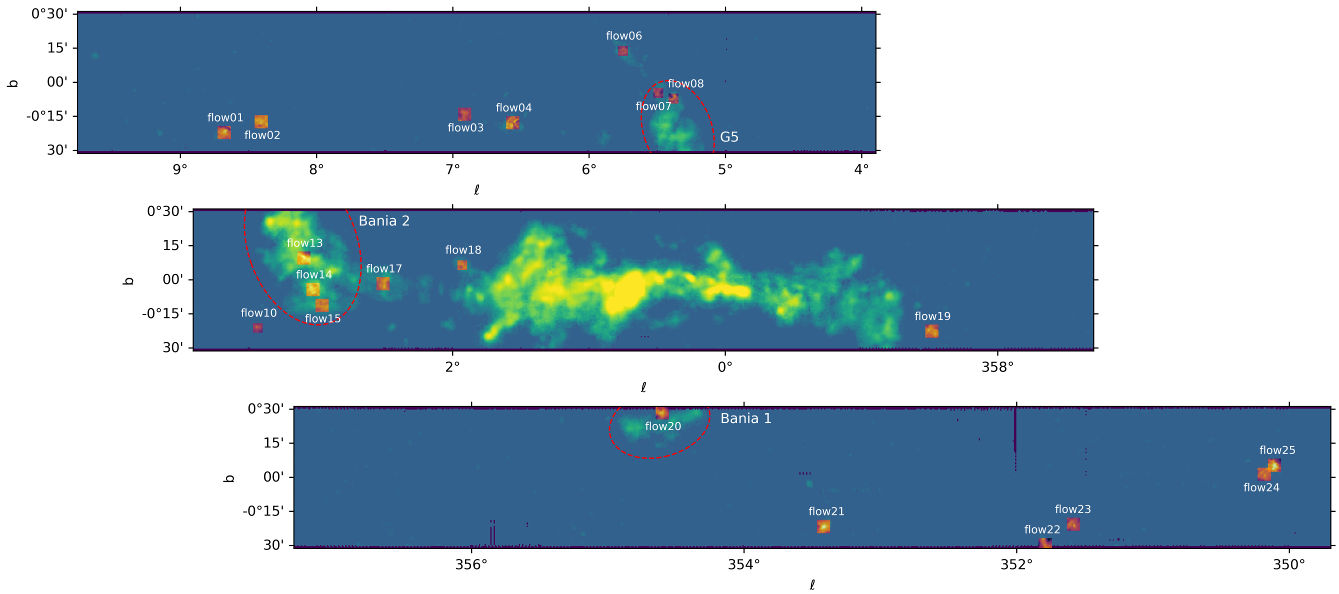

Figure 1. Spatial distribution of the 25 molecular clouds. The background is NH_3 (3,3) from the Mopra HOPS survey (Walsh et al. 2011; Purcell et al. 2012; Longmore et al. 2017). The overlays are our ^{13}CO $J = 2 \to 1$ moment 0 maps from ALMA. The clouds G5 at $(\ell, b) = (+5.4, -0.4)$, Bania 1 (Bania et al. 1986) at $(\ell, b) = (-5.4, +0.4)$, and Bania 2 (Stark & Bania 1986) at $(\ell, b) = (+3, +0.2)$ are circled in red.

Spectral Line	Rest Frequency (GHz)	Bandwidth	No. of Channels
SiO $J = 5 \to 4$	217.10498	0.25	512
H_2CO $J = 3_{21} \to 2_{20}$	218.760066	0.25	512
H_2CO $J = 3_{03} \to 2_{02}$	218.222192	0.25	512
HC_3N $J = 24 \to 23$	218.324723	0.25	512
CH_3OH $J = 4_{22} \to 3_{12}$	218.44005000		
$C^{18}O$ $J = 2 \to 1$	219.560358	0.25	1024
^{13}CO $J = 2 \to 1$	220.3986842	0.25	1024
^{12}CO $J = 2 \to 1$	230.538	0.25	2048
H(30)α	231.9009278	2	2048

Table 2. Observing parameters for each spectral window.

where N is the number of channels integrated over for the moment 0 map and $\Delta v = 0.332$ km s^{-1} is the velocity resolution. We then calculated ratio maps between each of the lines and both ^{12}CO $J = 2 \to 1$ and ^{13}CO $J = 2 \to 1$ using the respective moment 0 maps and the peak intensity maps. For each moment 0 ratio map, we calculate a corresponding error map, where the error dR is

$$dR = R\sqrt{\left(\frac{\sigma_1}{M_1}\right)^2 + \left(\frac{\sigma_2}{M_2}\right)^2} \tag{3}$$

where $M_i = \int I_v dv$ is the integrated intensity of line i, σ_i is the error of the moment 0 map (Eq. 2), and $R = \frac{M_1}{M_2}$ is the ratio between lines 1 and 2. We note that although σ is assumed to be constant across each moment 0 map (i.e. the rms of each pixel is assumed to be the same), the ratio error maps are not constant since they are also functions of the individual moment 0 maps as well. The same holds for the temperature error maps described in Section 3.

We also create position-velocity (PV) diagrams for each cube using the packages `pvextractor` and `spectral-cube` (Ginsburg et al. 2019). We select a path going through the main regions of each cloud, then calculate the PV diagram using the cloud velocity range, with an extra 10 km s^{-1} on each side.

All clouds display clear emission for all three carbon monoxide isotopologues, though some other lines do not have a significant detection. The detected lines for each cloud are shown in Table 3.

2.3. *Ancilllary Data*

Cloud No.	SiO	H_2CO $(3_{21}-2_{20})$	H_2CO $(3_{03}-2_{02})$	HC_3N	CH_3OH	H(30)α	NH_3 $(2,2)$	NH_3 $(6,6)$
1	✓	✓	✓	✓	✓	✓	✓	
2	✓	✓	✓		✓		✓	
3	✓	✓	✓		✓		✓	
4	✓	✓	✓	✓	✓		✓	
6	✓		✓		✓		✓	
7			✓					
8	✓	✓	✓		✓		✓	
10	✓	✓	✓	✓	✓	✓	✓	
13	✓	✓	✓	✓	✓		✓	✓
14	✓	✓	✓	✓	✓		✓	✓
15	✓	✓	✓		✓		✓	✓
17	✓	✓	✓		✓		✓	✓
18	✓	✓	✓		✓		✓	
19	✓	✓	✓	✓	✓		✓	
20	✓	✓	✓	✓	✓	✓	✓	
21	✓	✓	✓	✓	✓	✓	✓	
22	✓	✓	✓	✓	✓	✓	✓	
23	✓	✓	✓	✓	✓	✓	✓	
24	✓	✓	✓		✓	✓	✓	
25	✓	✓	✓	✓	✓	✓	✓	

Table 3. Lines detected in each cloud. ^{12}CO $J=2\rightarrow1$, ^{13}CO $J=2\rightarrow1$, $C^{18}O$ $J=2\rightarrow1$, NH_3 $(1,1)$, and NH_3 $(3,3)$ were detected in all clouds.

2.3.1. *HOPS*

We use the H_2O Southern Galactic Plane Survey (HOPS) (Walsh et al. 2011; Purcell et al. 2012; Longmore et al. 2017) for measurements of metastable ammonia inversion transitions with $(J,K)=(1,1),(2,2),(3,3)$ and $(6,6)$, for which the rotational temperature is similar to the gas kinetic temperature (Ott et al. 2005; Huettemeister et al. 1995). HOPS used the 22 m Mopra radio telescope, which has a main beam FWHM of 2' at 12 mm (Urquhart et al. 2010). Further observation details about the HOPS ammonia catalog can be found in Purcell et al. (2012).

The clouds were all initially selected to be bright in NH_3 $(3,3)$ emission and all clouds were observed in the NH_3 $(1,1)$, though not all clouds had significant NH_3 $(2,2)$ or $(6,6)$ emission. The ammonia line detections are also shown in Table 3. For each cloud, we select a region that covers the full extent of the cloud, which in general is larger than the ALMA FOV of the cloud. We then make a moment 0 map of each region for all four ammonia lines using the same velocity range as used for the ALMA moment maps.

2.3.2. *Spitzer*

We additionally use data from two *Spitzer* Galactic plane surveys, the Galactic Legacy Infrared Midplane Survey Extraordinaire (GLIMPSE; Churchwell et al. 2009) and the Multiband Imaging Photometer Galactic Plane Survey (MIPSGAL; Rieke et al. 2004, Carey et al. 2009). We use the cutout service of the Infrared Science Archive (IRSA) to take 10' wide images containing the central location of each cloud in the 4.5 and 8 μm bands of the Infrared Array Camera (IRAC; Fazio et al. 2004) from GLIMPSE. We also take 30' wide images of the same locations in the 24 μm band of MIPS, then regrid to match the pixel spacing of the GLIMPSE data using the `reproject` package.

Emission at 8 μm, which is generally dominated by polycyclic aromatic hydrocarbons (PAHs), can be used as an indicator of star formation, because it traces free-free emission well (Rahman & Murray 2010; Cohen & Green 2001). Photoionization from UV sources, such as massive stars, gives rise to free-free emission, while UV photons at lower energies simultaneously excite PAHs, which then emit at several vibrational transitions, including several in the 8 μm band (Allamandola et al. 1989). Near the centers of star-forming regions, where PAHs may be destroyed by extreme UV (EUV) and X-ray photons (Povich et al. 2007), the 8μm band is weakened but continues to contain some dust continuum emission.

24 μm emission, which is dominated by thermal emission from hot dust, also indirectly traces star formation, though it probes deeper into HII regions than PAH emission (Watson et al. 2008).

3. GAS TEMPERATURES

We calculate gas temperatures for all of the clouds using emission from ammonia and formaldehyde.

3.1. *Ammonia Temperature*

We first calculate the rotational temperature using ammonia lines for each cloud following the same procedure outlined in Ott et al. (2005). Assuming the ammonia emission is optically thin, the column density of an ammonia inversion doublet can be calculated as

$$N(J,K) = \frac{7.77\times10^{13}}{\nu}\frac{J(J+1)}{K^2}\int T_{\rm B}dv \tag{4}$$

(Henkel et al. 2000), where the column density N, rest frequency ν, and integrated main-beam brightness temperature have units cm^{-2}, GHz, and K km s^{-1}, respectively. We have only metastable ($J = K$) inversions, and the rotational temperature between two such states can be found from the equation

$$\frac{N(J',J')}{N(J,J)} = \frac{g_{\rm op}(J')}{g_{\rm op}(J)}\frac{2J'+1}{2J+1}\exp\left(\frac{-\Delta E}{T_{JJ'}}\right) \tag{5}$$

where ΔE is the energy level difference between the NH_3 (J', J') and NH_3 (J, J) transitions in K, and $g_{\rm op} = 1$ for para-ammonia (i.e. NH_3 $(1, 1)$ and $(2, 2)$) and $g_{\rm op} = 2$ for ortho-ammonia (i.e. NH_3 $(3, 3)$ and $(6, 6)$).

Solving for the rotational temperature gives

$$T_{JJ'} = \frac{-\Delta E}{\ln\left(\frac{N(J',J')}{g_{\rm op}(J')(2J'+1)}\right) - \ln\left(\frac{N(J,J)}{g_{\rm op}(J)(2J+1)}\right)} \tag{6}$$

For each cloud, we calculate a temperature map of T_{12}, T_{13}, and T_{36}, or the largest possible subset of the three given that some clouds do not have significant NH_3 $(3, 3)$ or $(6, 6)$ emission, by applying Eqs. 4 - 6 to the pairs of ammonia moment 0 maps, as well as a 5σ cutoff (Eq. 2 on both moment 0 maps. We also calculate ammonia temperature error maps,

$$dT_{JJ'} = \frac{T^2}{\Delta E}\sqrt{\left(\frac{dN(J',J')}{N(J',J')}\right)^2 + \left(\frac{dN(J,J)}{N(J,J)}\right)^2} \tag{7}$$

$$dN(J,K) = \frac{7.77\times10^{13}}{\nu}\frac{J(J+1)}{K^2}\sigma$$

where σ is the error of the integrated intensity map (Eq. 2). The ammonia temperature and error maps for all clouds are shown in Figure 2

To get a single temperature value for each pair of ammonia lines, we take the temperature and error at the brightest pixel in NH_3 (3, 3) moment 0 map. We show rotation diagrams (or Boltzmann diagrams) of the ammonia lines and the resultant temperature values in Figure 3

3.2. *Formaldehyde Temperature*

Next, we calculate the gas temperature based on the line ratio of H_2CO $(3_{21} - 2_{20})$ to H_2CO $(3_{03} - 2_{02})$. We take the ratio between the integrated intensity maps of the two lines, described in Section 2.2, enforcing a 3σ cutoff (Eq. 2) on both moment 0 maps. We then use the formula

$$T_G = 590R_{H_2CO}^2 + 2.88R_{H_2CO} + 23.4 \tag{8}$$

which is a polynomial fit to the gas temperature and formaldehyde line ratio $R_{H_2CO} = \frac{\int I_v(3_{21}-2_{20})dv}{\int I_v(3_{03}\to 2_{02})dv}$ (Ginsburg et al. 2016) derived from the radiative transfer code RADEX (Tak et al. 2007). This fit uses an assumed gas density of $n(H_2) = 10^4$ cm^{-3}, though the gas temperature has only a weak dependence on the assumed density. The resultant formaldehyde temperature and error maps are shown in Figure 4. We also calculate temperature error maps,

$$dT_G = 1080RdR + 2.88dR \tag{9}$$

where dR is the error on the formaldehyde ratio (Eq. 3).

Ideally, we would like to calculate the formaldehyde temperature at the same spatial location as the ammonia temperature. To do so, we return to the formaldehyde data cubes and regrid them to the same spatial and velocity resolution as the HOPS ammonia cubes. We create a regridded temperature map using the same procedure as above, then take the temperature (Eq. 8) and error (Eq. 9) at the pixel with peak NH_3 $(3, 3)$ integrated intensity.

We find that the peak NH_3 $(3, 3)$ pixel often lies far from the peak emission of the formaldehyde lines, and in one case lies outside the ALMA FOV of the corresponding cloud. We thus also calculate a potentially more representative formaldehyde temperature value by taking the mean of the temperature map at its original resolution within a 1' box centered on the pixel with maximum H_2CO $J = 3_{03} \to 2_{02}$ integrated intensity (light blue boxes in Figure 4). We take the error on this temperature to be the mean of the temperature error map within the same box.

We use this same box to calculate representative values for other properties of the ALMA data, such as the linewidths (Section 3.4) and ratio maps.

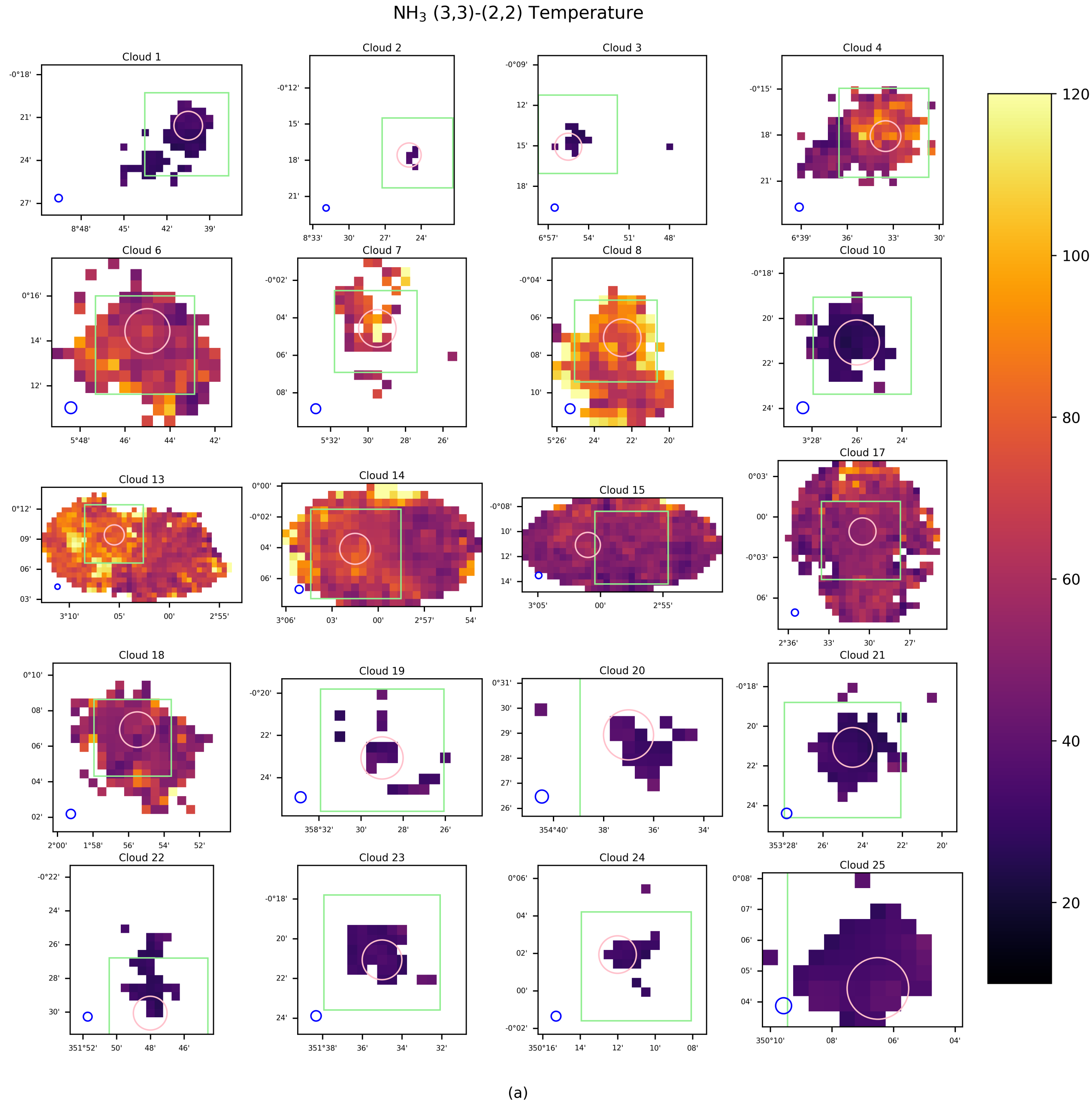

(a)

Figure 2. a) Ammonia temperature maps for each cloud, on the same color scale. The light green boxes indicate the ALMA FOV for the cloud. The pink circle is the Mopra HOPS beam, centered on the pixel with peak NH_3 (3,3) integrated intensity. The blue circles indicate the ALMA beamsize for comparison. *continued on next page*

3.3. *Ammonia vs. Formaldehyde Temperature*

A direct, quantitative comparison between the ammonia and formaldehyde temperature measurements is difficult because of the large difference in beamsize between the HOPS and ALMA data and the spatial distance between the peak NH_3 (3,3) and H_2CO $J = 3_{03} \rightarrow 2_{02}$ emission. We still plot the correlations between them in Figure 5, but we find no significant correlation between the ammonia and formaldehyde temperature. However, there is a clear correlation between the ammonia temperatures calculated using the NH_3 (1,1) and (2,2) emission versus that using the NH_3 (1,1) and (3,3) emission, as well as between the formaldehyde temperature taken at the pixel with peak NH_3 (3,3) emission versus that averaged over a 1' box centered at the peak H_2CO $J = 3_{03} \rightarrow 2_{02}$ emission, both of which are expected.

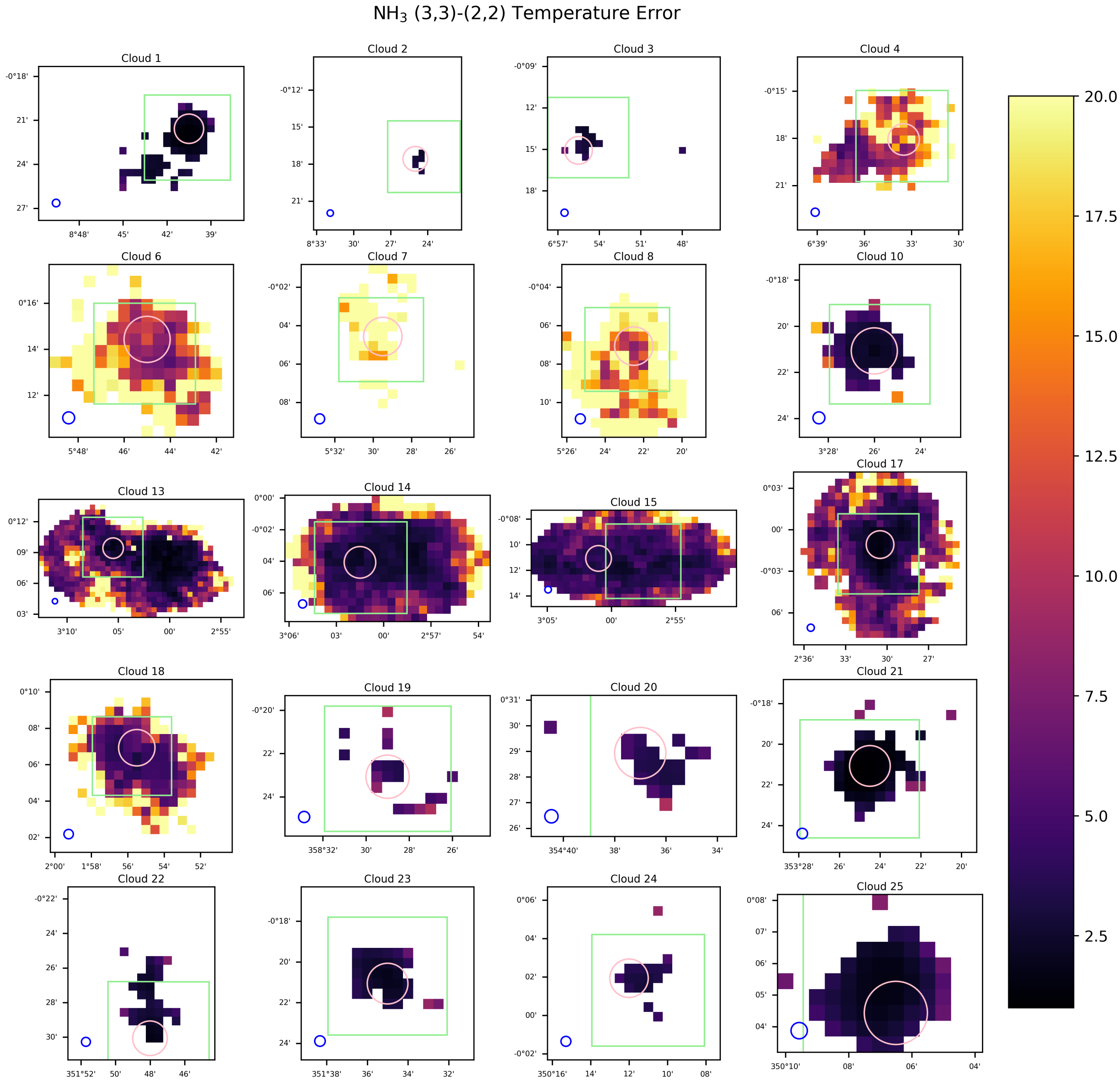

(b)

Figure 2. b) Ammonia temperature error maps for each cloud, with the same overlays as a).

The lack of any correlation between the ammonia and formaldehyde temperatures indicates they are likely tracing different gases. We compare the two thermometers in more detail in Section 5.2.

3.4. *Temperature vs. Linewidth*

We calculate a linewidth for each ALMA line by fitting a Gaussian to the mean spectrum of the 1' box centered on the peak pixel in the H_2CO $J = 3_{03} \rightarrow 2_{02}$ integrated intensity map. One cloud exhibits two components in its spectrum, so we fit a double Gaussian and take the wider of the two. Figure 6 shows that there is no correlation between the temperatures and linewidths of the clouds, which is expected if the line broadening is due to processes such as turbulence rather than thermal broadening. We can calculate the expected degree of thermal broadening for each cloud.

Assuming local thermal equilibrium, the thermal one-dimensional velocities of molecules should follow a Maxwell-Boltzmann distribution,

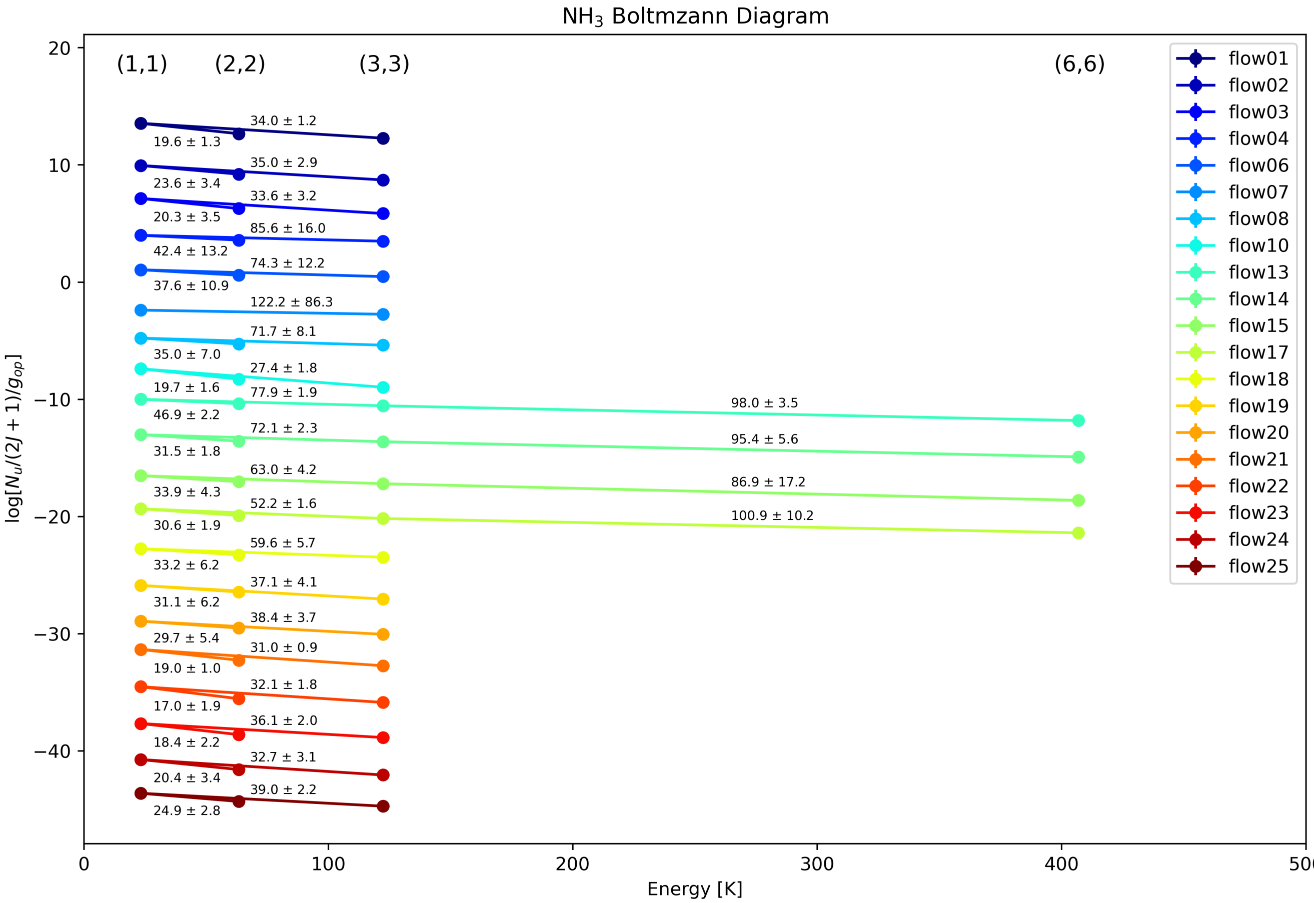

Figure 3. Ammonia emission Boltzmann diagrams for all clouds. The points for each cloud are shifted down 3 dex relative to the previous cloud.

$$f(v) = \left(\frac{\mu \, \mathrm{m_H}}{2\pi k_B T_k} \right)^{1/2} \exp\left(- \frac{\mu \, \mathrm{m_H} v^2}{2 k_B T_k} \right) \qquad (10)$$

where μ is the mean molecular weight of the gas, $\mathrm{m_H}$ is the mass of the hydrogen atom, k_B is Boltzmann's constant, and T_k is the kinetic temperature of the gas. The thermal FWHM is then

$$\Delta v_{\rm th} = \left(8 \ln 2 \frac{k_B T_k}{\mu m_H} \right)^{1/2} \qquad (11)$$

For formaldehyde, $\mu = 30$. Taking the calculated formaldehyde temperatures of each cloud to be representative of the kinetic temperature, we can calculate a thermal linewidth, then calculate a nonthermal linewidth corresponding to large- and small-scale velocity variations and motions, using

$$\Delta v_{\rm nth} = \sqrt{\Delta v^2 - \Delta v_{\rm th}^2} \qquad (12)$$

The nonthermal linewidths are significantly greater than the thermal linewidths, which range from $\sim$ 0.2-0.5 km s^{-1}, indicating that the gas is dominated by turbulence and other non-thermal motions.

The FWHM linewidths of formaldehyde in the clouds ranges between $\sim$4-50 km s^{-1}. The molecular clouds in the Galactic disk studied by Larson (1981) have a three-dimensional rms velocity dispersion between $\sim$0.4-9 km s^{-1}. The one-dimensional FWHM and three-dimensional rms velocity dispersions are related by

$$\Delta v_{1/2} = \sqrt{8 \ln 2/3} \, v_{\rm rms} \qquad (13)$$

The rms velocity dispersion range of our clouds is $\sim$3-40 km s^{-1}, with an average of 9.3 km s^{-1}, which lies between the values expected of clouds in the Galactic disk and clouds in the CMZ, the latter of which have FWHM linewidths on the order of 10-50 km s^{-1} (eg. Tsuboi et al. 2015). This suggests that our cloud sample may be intermediate between the clouds of the Galactic disk and the clouds in the extreme conditions of the CMZ.

We can approximate the sound speed of the cloud by assuming an isothermal gas with equation of state $P = \rho k_B T/(\mu \mathrm{m_H})$, in which case the sound speed is

$$\mathrm{c}_s = \sqrt{k_B T_k / \mu \mathrm{m_H}} \qquad (14)$$

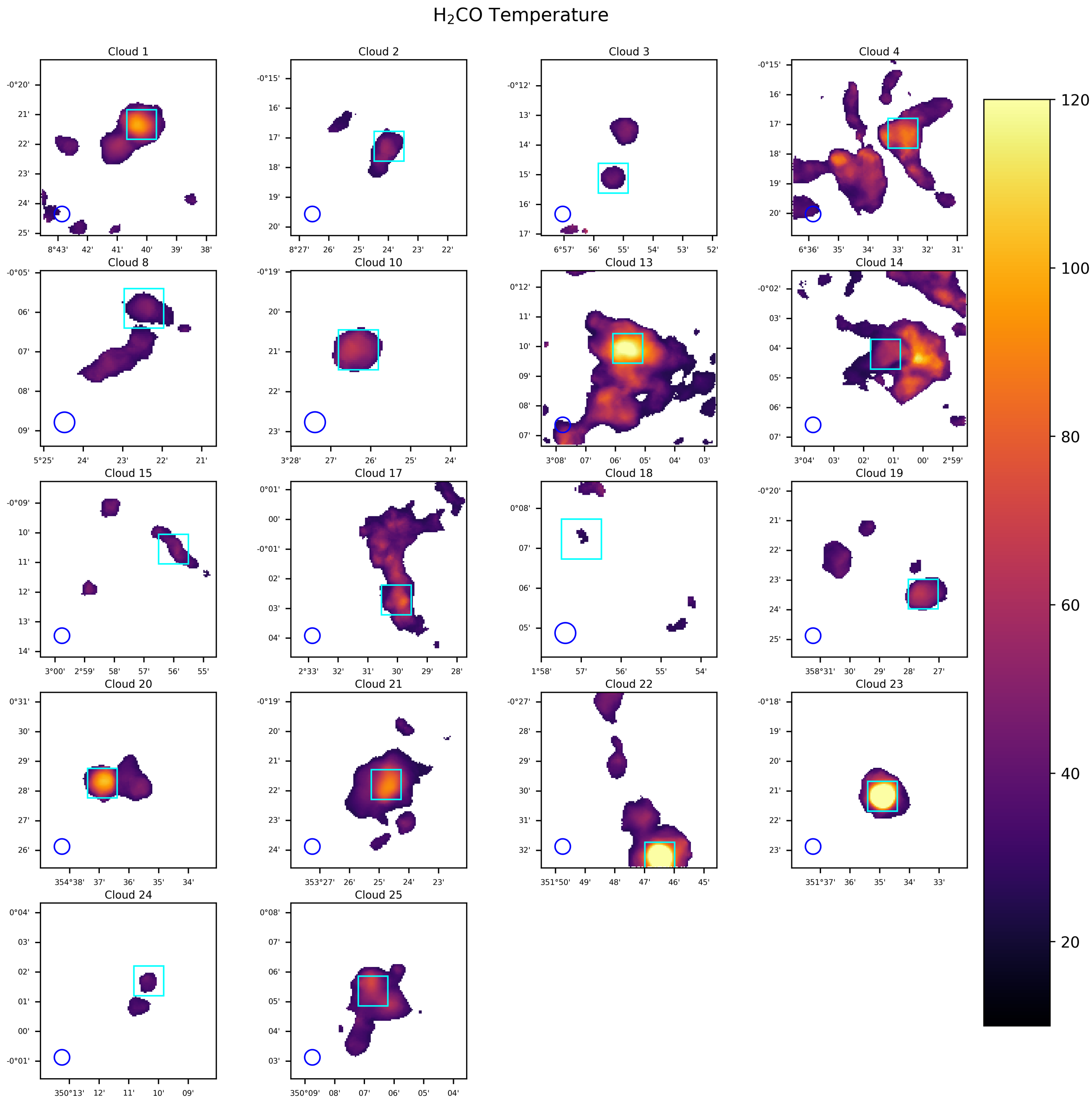

(a)

Figure 4. Formaldehyde temperature maps for each cloud, on the same color scale. The light blue boxes are 1' boxes centered on the pixel with peak H$_2$CO $J = 3_{03} \rightarrow 2_{02}$ integrated intensity. The blue circles indicate the beamsize. Clouds 6 and 7 do not show any H$_2$CO $J = 3_{21} \rightarrow 2_{20}$ emission and thus do not have formaldehyde temperature maps. *continued on next page*

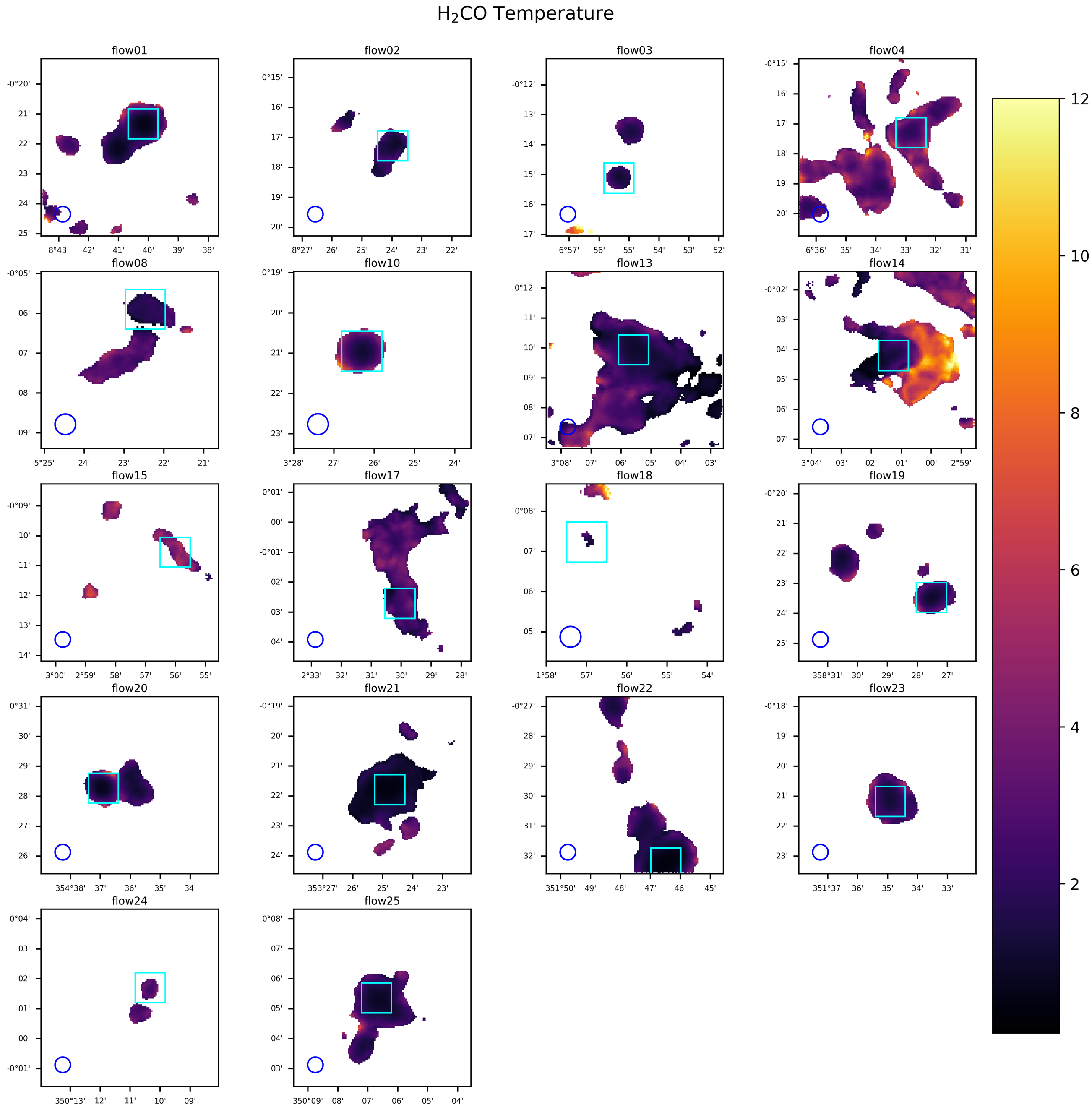

(b)

Figure 4. b) Formaldehyde temperature error maps for each cloud, with the same overlays as a).

where $\mu = 2.34$ is now the mean molecular weight of a molecular cloud (Syed et al. 2020). The three-dimensional Mach number, assuming isotropic turbulence, is then $\mathcal{M} = v_{\rm rms}/c_s$, where $v_{\rm rms}$ is the non-thermal three-dimensional rms velocity dispersion of Eq. 13. The calculated Mach numbers range from 7 to 45, with an average of 18.7 ± 12.7. These values also lie between those typical of molecular clouds in the Galactic disk ($\lesssim 5$; eg. Tang et al. 2018, Syed et al. 2020) and those observed in the CMZ ($\gtrsim 25$; eg. Kauffmann et al. 2017, Henshaw et al. 2016).

We take the errors in the total linewidths to be the errors on the Gaussian fits, then propagate accordingly to get errors on the Mach numbers.

3.5. *Star Formation*

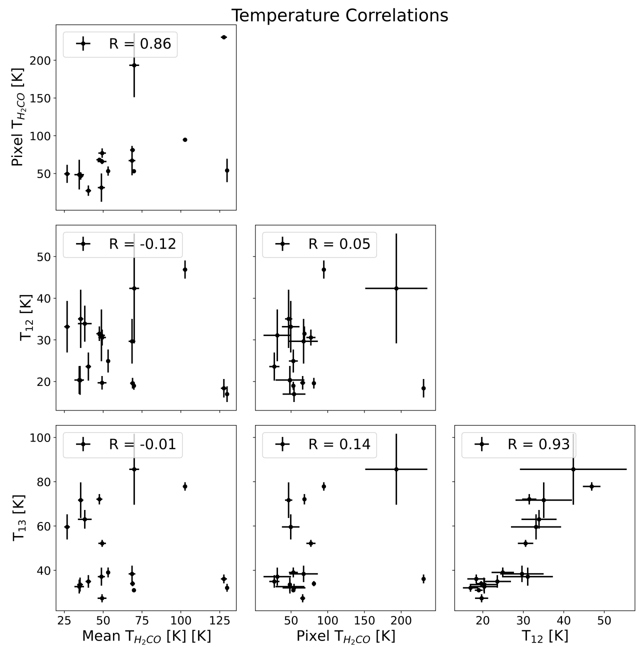

Figure 5. Correlations between different temperature measures. Mean T_{H_2CO} denotes the average formaldehyde temperature within a 1' box centered on the pixel with peak H_2CO $J = 3_{03} \rightarrow 2_{02}$ integrated intensity, whereas Pixel T_{H_2CO} denotes the formaldehyde temperature at the pixel with maximum NH_3 (3,3) integrated intensity once regridded to the ammonia resolution. T_{12} represents the ammonia temperature calculated using NH_3 (1,1) and (2,2), taken at the pixel with peak NH_3 (3,3) integrated intensity, and T_{13} is the ammonia temperature calculated using NH_3 (1,1) and (3,3) at the same pixel.

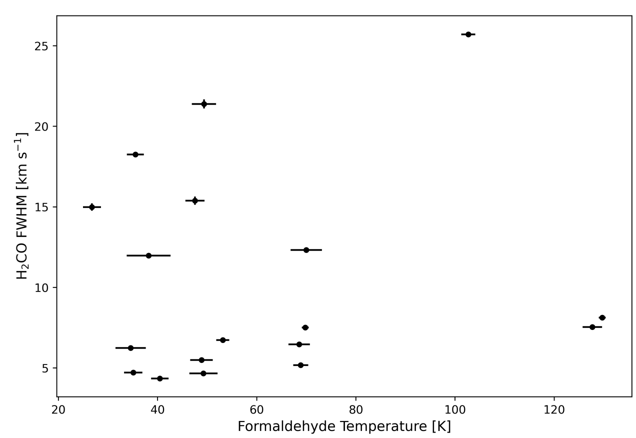

Figure 6. H_2CO FWHM linewidth against formaldehyde temperature. Both are calculated over a 1' box centered on the pixel with peak H_2CO $J = 3_{03} \rightarrow 2_{02}$ emission.

We can calculate the ionizing photon production rate, Q, from measurements of H30α, via

$$\frac{Q(\mathrm{H}n\alpha)}{\mathrm{s}^{-1}} = 3.99 \times 10^{24} \left(\frac{\alpha_B}{\mathrm{cm}^3\ \mathrm{s}^{-1}}\right) \left(\frac{\epsilon_\nu}{\mathrm{erg\ s}^{-1}\ \mathrm{cm}^{-3}}\right)^{-1} \times \left(\frac{\nu}{\mathrm{GHz}}\right) \left(\frac{D}{\mathrm{kpc}}\right)^2 \left(\frac{\int F_\nu dv}{\mathrm{Jy\ km\ s}^{-1}}\right) \tag{15}$$

(Scoville & Murchikova 2013; Bendo et al. 2017; Kim et al. 2018) where α_B is the effective recombination coefficient and ϵ_ν is the emissivity, both of which are functions of electron density and temperature.

To estimate the electron temperature, we use the Galactic disk electron temperature gradient from Quireza et al. (2006),

$$T_e = (5780 \pm 350) + (287 \pm 46) R_{\mathrm{Gal}}[\mathrm{kpc}] \tag{16}$$

which is an empirical fit to H II regions with electron temperatures derived from radio recombination line and continuum measurements, and Galactocentric distances calculated via radial velocity measurements. However, we can also set an upper limit on the electron temperature using the linewidth of our H30α observations. The thermal contribution to the linewidth is Gaussian and has a FWHM of

$$\Delta v_{\mathrm{th}} = \left(8 \ln 2 \frac{k_{\mathrm{B}} T_e}{m_{\mathrm{H}}}\right)^{1/2} \tag{17}$$

(Rivera-Soto et al. 2020), which is the same form as Eq. 11 but replacing the kinetic temperature with electron temperature. Since the H30α is at a high enough frequency for pressure broadening, which is proportional to ν^{-4}, to be negligible (Keto et al. 2008), the total H30α line should be Gaussian and have a FWHM of

$$\Delta v = \sqrt{\Delta v_{\mathrm{th}}^2 + \Delta v_{\mathrm{dy}}^2} \tag{18}$$

where Δv_{dy} is the dynamical contribution from unresolved bulk motions. Thus, for the clouds whose electron temperature calculated from Eq. 16 is greater than the upper limit set by Eq. 17 (using the Gaussian linewidth calculated in Section 3.4), we instead use the latter as an upper limit on the electron temperature, with an error derived from the linewidth uncertainty of the Gaussian fit.

Whereas the value of the electron temperature can affect the ionizing photon production rate Q by a factor of up to ~2.5 over a temperature range from 3000 to 15000 K, the electron density has a relatively small effect on Q, with less than a 15% variation in both the recombination coefficient and emissivity over a density range from 10^2 and 10^5 cm^{-3} (Bendo et al. 2017). We estimate the electron density using the fits of n_e against diameter of galactic H II regions by Hunt & Hirashita

(2009). To calculate sizes for our clouds, we collapse the H30α PV diagram along the velocity axis to create a 1D cloud profile, then fit a Gaussian. We take the angular diameter of the cloud to be 4σ, then calculate a physical size using the distance to the cloud, assuming it lies on the Galactic bar. The resulting cloud sizes all lie within the range of 1 and 10 pc, which is covered by the Kim et al. (2018) sample of compact Galactic HII regions; Hunt & Hirashita finds a best-fit regression of

$$\log\, n_e\ [\mathrm{cm}^{-3}] = 2.8 - \log\, D\ [\mathrm{pc}] \tag{19}$$

Using these calculated electron densities and temperatures, we interpolate the tables of α_B and ϵ_ν values published by Storey & Hummer (1995). We calculate errors on these values using a simple Monte Carlo simulation, assuming a normal distribution for T_e and n_e. To calculate the integrated flux density of H30α from our moment 0 maps, we use a 1' box centered on the pixel with peak H30α integrated intensity, then take

$$\int F_v\ dv\ [\mathrm{Jy\ km\ s^{-1}}] = \frac{2k_B\nu^2}{c^2}\iint T_B\ dv\ d\Omega \tag{20}$$

where $\int T_B\ dv$ is the moment 0 map.

The quantities derived from the H30α line, including the ionizing photon production rate Q, are shown for all the clouds with H30α detection in Table 4. The resultant Q values are all consistent, within error bars, with O stars, which have $\log_{10}Q$ values between 47.88 for an O9.5 star and 49.64 for a an O3 star (Martins et al. 2005).

We also calculate upper limits on Q values for the clouds without significant H30α detections. We take the upper limit on the integrated flux density to be

$$\int F_v\ dv\ [\mathrm{Jy\ km\ s^{-1}}] \leq \frac{2k_B\nu^2}{c^2}\sigma\sqrt{N} \tag{21}$$

where σ is the error on the H30α moment 0 map (2) and N is the number of pixels in a 1' box on the map. We use the electron temperature gradient (16) to estimate electron temperatures for each cloud, and use the mean of the electron densities of clouds with H30α detections as an estimate for the electron density of clouds with no detection. We use an α_B and ϵ_ν value interpolated from the electron temperature and density and calculate a photoionizing photon production rate using Eq. 15; we take a 2σ upper limit of twice this Q value. The same method is used to calculate errors on the Q values for clouds with H30α emission.

Figure 7 shows that there is generally a correlation between the presence and location of H30α and both 8 μm and 24 μm emission, though there are also a few clouds with 24 μm emission consistent with the location of formaldehyde emission that do not display any emission in H30α. We can estimate the star formation rate in the clouds from 24 μm emission using the relationship from Calzetti et al. (2007),

$$\mathrm{SFR}\ [\mathrm{M_\odot\ yr^{-1}}] = 1.27\times10^{-38}(L_{24\mu\mathrm{m}}\ [\mathrm{ergs\ s^{-1}}])^{0.8850} \tag{22}$$

where $L_{24\mu\mathrm{m}} = \nu L(\nu)$. This relation is derived from extragalactic star-forming regions, so may not be fully applicable to our clouds. For comparison, we also calculate a star formation rate from the ionizing photon production rate using a conversion from Q to SFR of $7.29\times10^{-54}\ \mathrm{M_\odot yr^{-1}/s^{-1}}$ (Murphy et al. 2011), which is calculated using `STARBURST99` (Leitherer et al. 1999) and also applies primarily to the galactic scale. It also assumes solar metallicity and a constant SFR over about 100 Myr.

The 24 μm MIPSGAL processing pipeline masks artifacts in the data, which are particularly prevalent around bright sources (Mizuno et al. 2008). Most of the clouds with H30α emission, which are also bright in the mid-IR, are thus masked, as can be seen in Figure 7. To mitigate this effect, we interpolate the missing values, though this is imperfect as the masked pixels are generally around the brightest locations.

We integrate the 24 μm emission, which is given in units of MJy/sr, over a 2' box centered on the location with peak H30α integrated intensity. We choose a larger box size than for calculating the H30α flux density because we expect the emission to be more extended, as the 24 μm emission comes from dust around the star-forming region whereas H30α emission comes from, or closer to, the ionized region. We convert these fluxes into luminosities using their distances, then calculate the SFR with Eq. 22.

To calculate errors on the SFR of these clouds, as well as upper limits on the clouds with no detection, we use the uncertainty maps provided by MIPSGAL. For the clouds with detections, we add the pixel errors in quadrature over the integration box and multiply by the pixel spacing to get a flux density error; for the other clouds, we take the mean over the uncertainty map and multiply by the square root of the number of pixels in a 2' box and the pixel spacing. We then propagate the distance error and the errors in the parameters of Eq. 22 appropriately to get an error. We again use a 2σ detection as an upper limit.

A comparison between the two SFR measures is shown in Figure 8. The values generally agree, though using H30α tends to underestimate the SFR compared to value derived from 24 μm emission. We are also able to place stricter upper limits using H30α.

Cloud No.	Δv [km s^{-1}]	T_e [K]	$d_{\rm H30\alpha}$ [pc]	n_e [cm$_{-3}$]	$\int F_v dv$ [Jy km s^{-1}]	$\log_{10}Q$ [s^{-1}]
1	27.21 ± 1.04	6346.62 ± 362.44	1.85 ± 0.35	341.40 ± 64.64	28.94 ± 0.07	48.28 ± 0.14
20	38.99 ± 2.09	6310.61 ± 362.45	3.51 ± 0.49	179.77 ± 25.03	5.50 ± 0.05	47.90 ± 0.12
21	26.62 ± 0.22	6457.10 ± 370.49	5.36 ± 0.68	117.70 ± 15.03	147.07 ± 0.08	49.37 ± 0.12
22	10.18 ± 0.81	$\leq 2267.33 \pm 359.82$	2.50 ± 0.35	252.32 ± 34.97	13.31 ± 0.17	48.10 ± 0.17
23	25.41 ± 1.07	6713.92 ± 389.49	3.63 ± 0.46	173.90 ± 21.97	61.63 ± 0.06	49.07 ± 0.12
24	26.62 ± 1.78	6939.81 ± 411.34	4.92 ± 0.68	128.36 ± 17.80	1.95 ± 0.05	47.64 ± 0.12
25	28.15 ± 0.24	6952.76 ± 412.73	4.13 ± 0.54	152.65 ± 19.84	135.03 ± 0.10	49.48 ± 0.12

Table 4. H30α derived quantities.

Calzetti et al. (2007) notes that emission at 8 μm. while correlated with star formation, also depends strongly on metallicity and size, so we do not calculate a SFR using the 8 μm emission from GLIMPSE. We note, however, that 8 μm emission is present for all clouds that exhibit 24 μm emission.

4. SHOCKS

Both methanol (CH_3OH) and SiO are associated with the presence of shocks (Meier & Turner 2005; Schilke et al. 1997), though they trace different shock velocities. CH_3OH can be formed through grain mantle evaporation, which may result from weak shocks with $v_s \lesssim 10$ km s^{-1} (Bergin et al. 1998). On the other hand, SiO formation requires more energetic grain processing through grain core or mantle erosion, which can occur in shocks with $v_s \gtrsim 25$ km s^{-1} (Garay et al. 2000).

SiO and CH_3OH are both detected in all clouds except cloud 7.

4.1. *SiO*

We can calculate the column density of SiO, with several assumptions. We assume optically thin emission, LTE, a Rayleigh-Jeans approximation, and negligible background. Then, the column density is

$$N_{\rm tot} = \left(\frac{3k_B}{8\pi^3 \nu S \mu^2}\right)\left(\frac{Q_{\rm rot}}{g_J g_K g_I}\right)\exp\left(\frac{E_u}{k_B T_{\rm ex}}\right)\int \frac{T_B dv}{f} \tag{23}$$

(Mangum & Shirley 2015), where $Q_{\rm rot}$ is the partition function, g_i are the degeneracies, μ is the dipole moment of the molecule, S is the intrinsic line strength, E_u is the upper energy level, $T_{\rm ex}$ is the excitation temperature of the gas, and f is the beam filling factor. Assuming LTE, we have $T_{\rm ex} = T_{\rm k}$. Although the formaldehyde and SiO may not trace the same gas, we take the formaldehyde gas temperature to be the kinetic temperature of the SiO. For a linear molecule like SiO, we have $g_J = 2J+1$, $g_K = g_I = 1$, $Q_{\rm rot} = \sum_{J=0}^{\infty}(2J+1)\exp(-\frac{E_J}{kT})$, and $S = \frac{J}{2J+1}$. For a diatomic molecule, the rotational energy levels are $E_J \approx hBJ(J+1)$, where $B = \frac{\hbar}{4\pi I}$ is the rotational constant of the molecule. For SiO in particular, the dipole moment is $\mu = 3.0982$ Debye (Raymonda et al. 1970) and the rotational constant is $B = 21787.5$ MHz (Lowry Manson et al. 1977). We assume the beam filling factor is 1.

We use the average integrated intensity of SiO $J = 5 \rightarrow 4$ within the same 1' box that the formaldehyde temperature is calculated in to derive column density values. We note that the minimum formaldehyde temperature across the clouds is about 25 K, and at a frequency of 217 GHz, so Figure 3 of Mangum & Shirley (2015) tells us to expect that our column density calculations with the Rayleigh-Jeans approximation and assuming negligible background should agree within 1% to column densities calculated without these assumptions (though still assuming optically thin emission and LTE) for the majority of the clouds.

We also calculate column densities of ^{13}CO and C^{18}O $J = 2 \rightarrow 1$ to obtain SiO abundances. Since it is likely these lines are optically thin, compared to their isotopologue ^{12}CO, we can again use Eq. 23. CO is also a linear, diatomic molecule, so the only changes apart from the frequency are the dipole moments and rotational constants of the molecules, which are $\mu = 0.11046$ Debye and $B = 55101.011$ MHz for ^{13}CO, and are $\mu = 0.11079$ Debye and $B = 54891.420$ MHz for C^{18}O[1].

The ^{12}C/^{13}C and ^{16}O/^{18}O isotope abundance ratios increase with Galactocentric radius (Langer & Penzias 1990). We use the equations

$$^{12}C/^{13}C = (7.5 \pm 1.9)R_{\rm Gal} + (7.6 \pm 12.9) \tag{24}$$

and

$$^{16}O/^{18}O = (58.8 \pm 11.8)R_{\rm Gal} + (37.1 \pm 82.6) \tag{25}$$

from Wilson & Rood (1994). The CO column densities derived from the two isotopologues agree well; the SiO abundances (N(SiO)/N(H_2)) derived from both are shown in Figure 9, where we have assumed a ^{12}CO to H_2 ratio of 10^{-4}.

[1] Values taken from https://spec.jpl.nasa.gov/

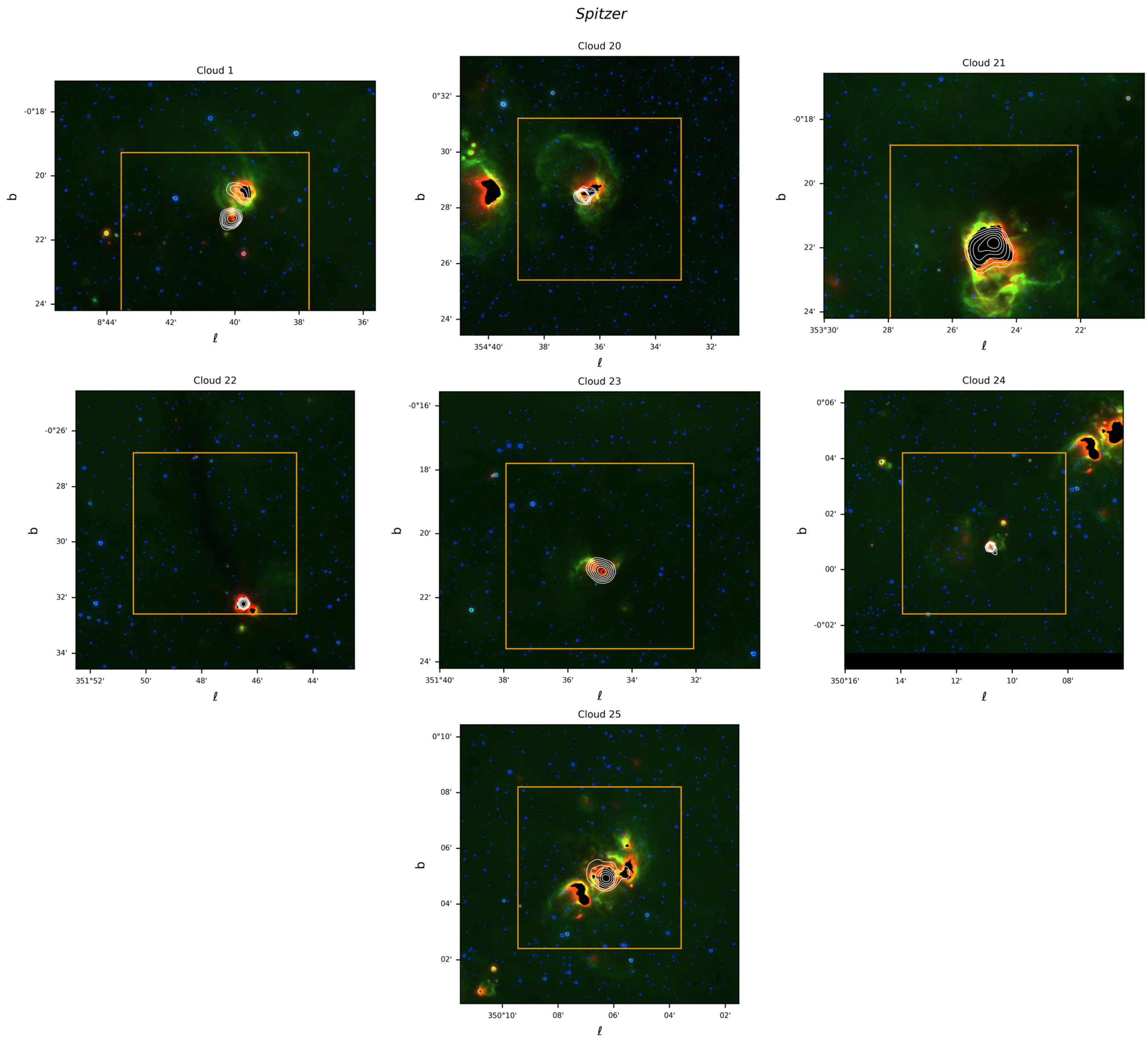

Figure 7. Three-color *Spitzer* images of the clouds with H30α emission, with GLIMPSE 4.5 μm, GLIMPSE 8 μm, and MIPSGAL 24 μm in blue, green, and red, respectively. The contours show H30α integrated intensity, and the orange boxes depict the ALMA FOV. The 24 μm data contains artifacts at bright spots, so they are masked by the MIPSGAL processing pipeline.

Shocks can enhance the abundance of SiO to values greater than 10^{-10} compared to ambient values of 10^{-12} to 10^{-11} (Schilke et al. 1997; Garay et al. 2000), and they have been shown to enhance abundances to values as high as 10^{-6} at extreme velocities (Martin-Pintado et al. 1992). Many of the clouds in our sample exhibit SiO abundances above 10^{-10}, with some exceeding 10^{-9}, indicating that the gas in these clouds are likely undergoing shocks.

4.2. *Methanol*

We use the line ratio of CH_3OH $J = 4_{22} \rightarrow 3_{12}$ to ^{13}CO $J = 2 \rightarrow 1$ to assess the weak shocks associated with methanol emission. We take the mean value of the 1' box centered on the pixel with peak H_2CO $J = 3_{03} \rightarrow 2_{02}$ emission, and we take the error to be the mean of the ratio error map within the same box.

Figure 10 shows that the methanol line ratio is well-correlated with the formaldehyde temperature, but it has no correlation with the ammonia temperature.

5. DISCUSSION

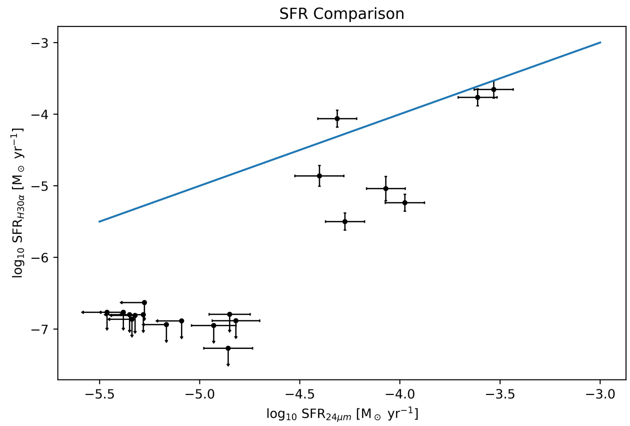

Figure 8. Comparison of SFR calculated using H30α emission versus that calculated using 24 μm emission from *Spitzer*. The blue line assumes the two are equal.

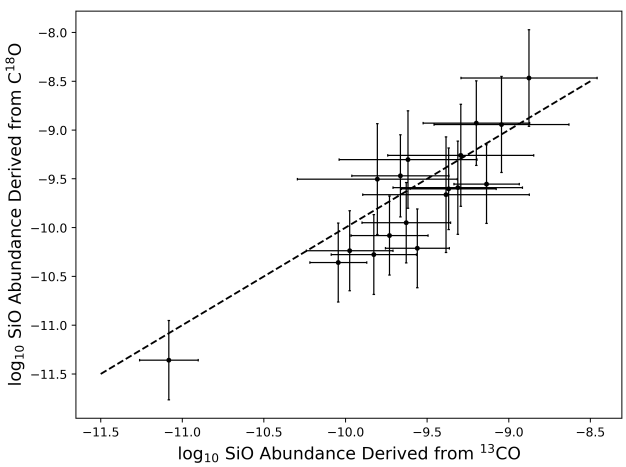

Figure 9. Comparison of SiO abundances calculated using the column density of ^{18}CO and ^{13}CO. The dashed black line assumes the two are equal. The two methods are consistent with each other, as expected.

5.1. *Galactocentric Radius*

We show the distribution of SFR, temperature, turbulent Mach number, and SiO abundance ratio on Galactocentric radius, assuming that the clouds lie on the bar, in Figure 11. Similarly, Figure 12 show the same properties as a function of position along the bar. We find that the SFR appears to be higher at further distances from the Galactic Center, with star formation largely inhibited for clouds closer to the Galactic Center. On the other hand, the clouds at a smaller Galactocentric radius appear to be more turbulent, which may be inhibiting star formation. There also appears to be a strong asymmetry between the SFR and turbulence of clouds on the near and far sides of the bar.

Temperature, traced by both ammonia and formaldehyde, appear to be less position dependent, as do shocks, traced by SiO abundance. This may be expected, as both turbulence and star formation can cause heating and shocks.

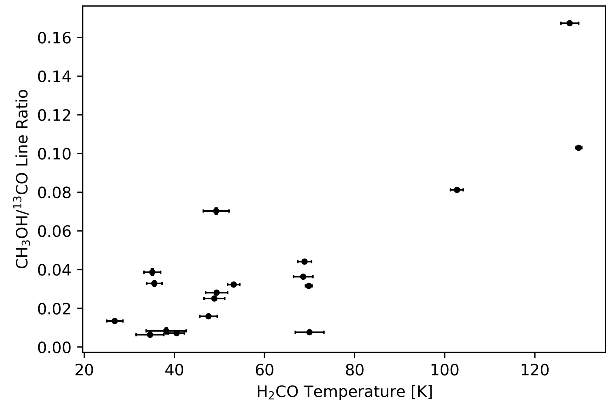

Figure 10. $CH_3OH/^{13}CO$ line ratio as a function of formaldehyde temperature.

However, while there is a known asymmetry in the CMZ (eg. Sormani et al. 2018), we do not expect it to be this prominent nor extend out to a radius of over 4 kpc. Additionally, our sample at $\ell < 0$ and $\ell > 0$ covers complementary Galactocentric radii, with the clouds at $\ell < 0$ mostly at $R_{\rm Gal} > 2$ kpc and clouds at $\ell > 0$ mostly at $0.5 < R_{\rm Gal} < 2$ kpc, which makes it difficult to directly compare all the clouds.

Figure 13 shows the uncertainty involved in the positions of the clouds in our sample. Even if all the clouds do lie on the Galactic bar, the clouds on the near and far sides of the bar are likely in different regions of the bar. In particular, the geometry on the far side of the bar is much more uncertain due to projection effects.

To determine whether or not the clouds do lie on the bar, we can look at the locations of the cloud on a longitude-velocity, or ℓ-v, diagram. This is shown in Figure 14. We see that many of the clouds are consistent with being in the Galactic disk, which is the generally flat feature at all longitudes around a velocity of 0 km/s, and the dust lane features are at higher velocities than all of our clouds. This indicates that the clouds are likely not in the Galactic bar. However, the groups of clouds around $\ell = 5.4°$ and $\ell = 2.5°$ appear to be associated with the cloud clumps G5 and B2, respectively. G5 may be the location of gas from the far side dust lane that has overshot the CMZ and is colliding with the near side dust lane, and B2 may be the location of gas in the near side dust line colliding with the CMZ itself (Sormani et al. 2018). The clouds in these associations may be the most interesting candidates for additional analysis.

Regardless of position, we find an inverse relationship

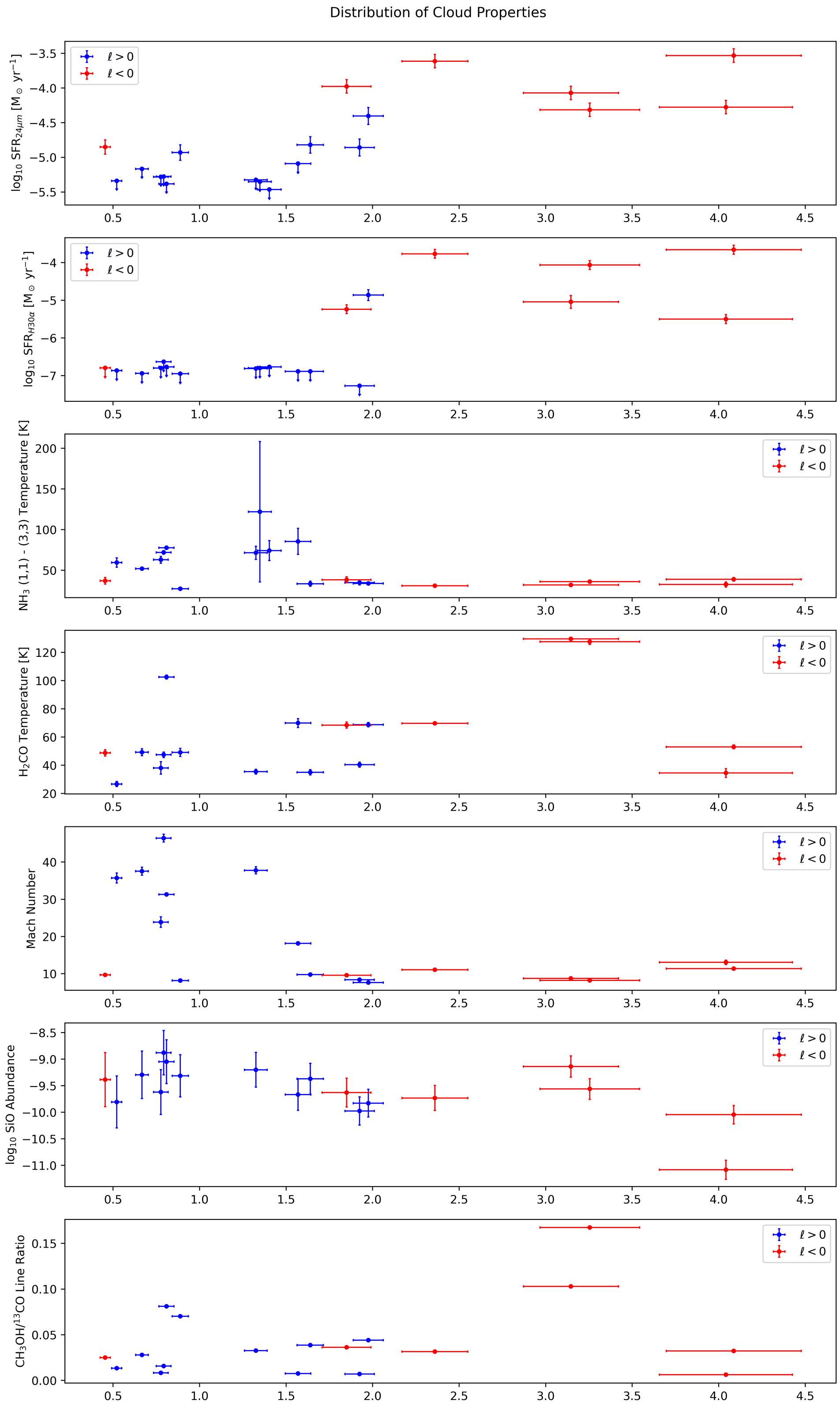

Figure 11. Distribution of properties as a function of Galactocentric distance.

between SFR and turbulent Mach number, which may support the idea that turbulence inhibits star formation.

5.2. *Temperature*

The formaldehyde and ammonia thermometers appear to be tracing different gas in the clouds. The ammonia temperature is well-correlated with the turbulent Mach number, whereas the formaldehyde temperature is not. On the other hand, the opposite is true for correlations with the $CH_3OH/^{13}CO$ line ratio, which is a weak shock tracer. Furthermore, the hot molecular cores seen in the formaldehyde temperature maps are generally not present in the ammonia temperature maps.

There are several possible reasons for this difference. It may be that formaldehyde is more sensitive to heating from star formation and that ammonia is more sensitive to turbulent heating. Formaldehyde may also be more sensitive to shock heating, or that shocks from SF enhance methanol abundance more than turbulent shocks do. Ammonia generally traces more diffuse gas than formaldehyde, so the difference may also be due to differences in the properties and kinematics of gas at different densities. More analysis is needed to better understand the relationships between the ammonia and formaldehyde thermometers.

6. CONCLUSION

We observed the molecular lines SiO $J = 5 \rightarrow 4$, H_2CO $J = 3_{21} \rightarrow 2_{20}$, H_2CO $J = 3_{03} \rightarrow 2_{02}$, HC_3N $J = 24 \rightarrow 23$, CH_3OH $J = 4_{22} \rightarrow 3_{12}$, $C^{18}O$ $J = 2 \rightarrow 1$, ^{13}CO $J = 2 \rightarrow 1$, ^{12}CO $J = 2 \rightarrow 1$, and H30α for 25 clouds in the inner Galactic disk outside the CMZ. These spectral lines probe several processes, and we measure temperatures, shocks, turbulence, and SFRs for all the clouds.

We find that the properties of the clouds are consistent with not being on the Galactic bar, but several of the clouds are likely associated with regions of high velocity gas collisions. These clouds in particular should be the subject of future study. We further find that turbulence may be inhibiting star formation in many of the clouds in our sample, and that the ammonia and formaldehyde temperatures may be tracing different gases, though further investigation is needed for these findings.

AN would like to thank Dr. Juergen Ott, Dr. David Meier, and Dr. Brian Svoboda for their research guidance, the National Radio Astronomy Observatory for the opportunity to complete this summer research, and Dr. Mattia Sormani for helpful discussion about the Galactic bar.

Software: Python, IPython (Perez & Granger 2007), NumPy (Harris et al. 2020), Matplotlib (Hunter 2007), SciPy (Virtanen et al. 2020), Astropy (The Astropy Collaboration et al. 2022) , `spectral-cube` (Ginsburg et al. 2019), CASA (The CASA Team et al. 2022)

REFERENCES

Abuter, R., Amorim, A., Bauböck, M., et al. 2019, Astronomy & Astrophysics, 625, L10, doi: 10.1051/0004-6361/201935656

Allamandola, L. J., Tielens, A. G. G. M., & Barker, J. R. 1989, The Astrophysical Journal Supplement Series, 71, 733, doi: 10.1086/191396

Bania, T. M., Stark, A. A., & Heiligman, G. M. 1986, The Astrophysical Journal, 307, 350, doi: 10.1086/164422

Bendo, G. J., Miura, R. E., Espada, D., et al. 2017, Monthly Notices of the Royal Astronomical Society, 472, 1239, doi: 10.1093/mnras/stx1837

Bergin, E. A., Melnick, G. J., & Neufeld, D. A. 1998, The Astrophysical Journal, 499, 777, doi: 10.1086/305656

Binney, J., Gerhard, O. E., Stark, A. A., Bally, J., & Uchida, K. I. 1991, Monthly Notices of the Royal Astronomical Society, 252, 210, doi: 10.1093/mnras/252.2.210

Bitran, M., Alvarez, H., Bronfman, L., May, J., & Thaddeus, P. 1997, Astronomy and Astrophysics Supplement Series, 125, 99, doi: 10.1051/aas:1997214

Bland-Hawthorn, J., & Gerhard, O. 2016, Annual Review of Astronomy and Astrophysics, 54, 529, doi: 10.1146/annurev-astro-081915-023441

Calzetti, D., Kennicutt, R. C., Engelbracht, C. W., et al. 2007, The Astrophysical Journal, 666, 870, doi: 10.1086/520082

Carey, S. J., Noriega-Crespo, A., Mizuno, D. R., et al. 2009, Publications of the Astronomical Society of the Pacific, 121, 76, doi: 10.1086/596581

Churchwell, E., Babler, B. L., Meade, M. R., et al. 2009, Publications of the Astronomical Society of the Pacific, 121, 213, doi: 10.1086/597811

Cohen, M., & Green, A. J. 2001, Monthly Notices of the Royal Astronomical Society, 325, 531, doi: 10.1046/j.1365-8711.2001.04421.x

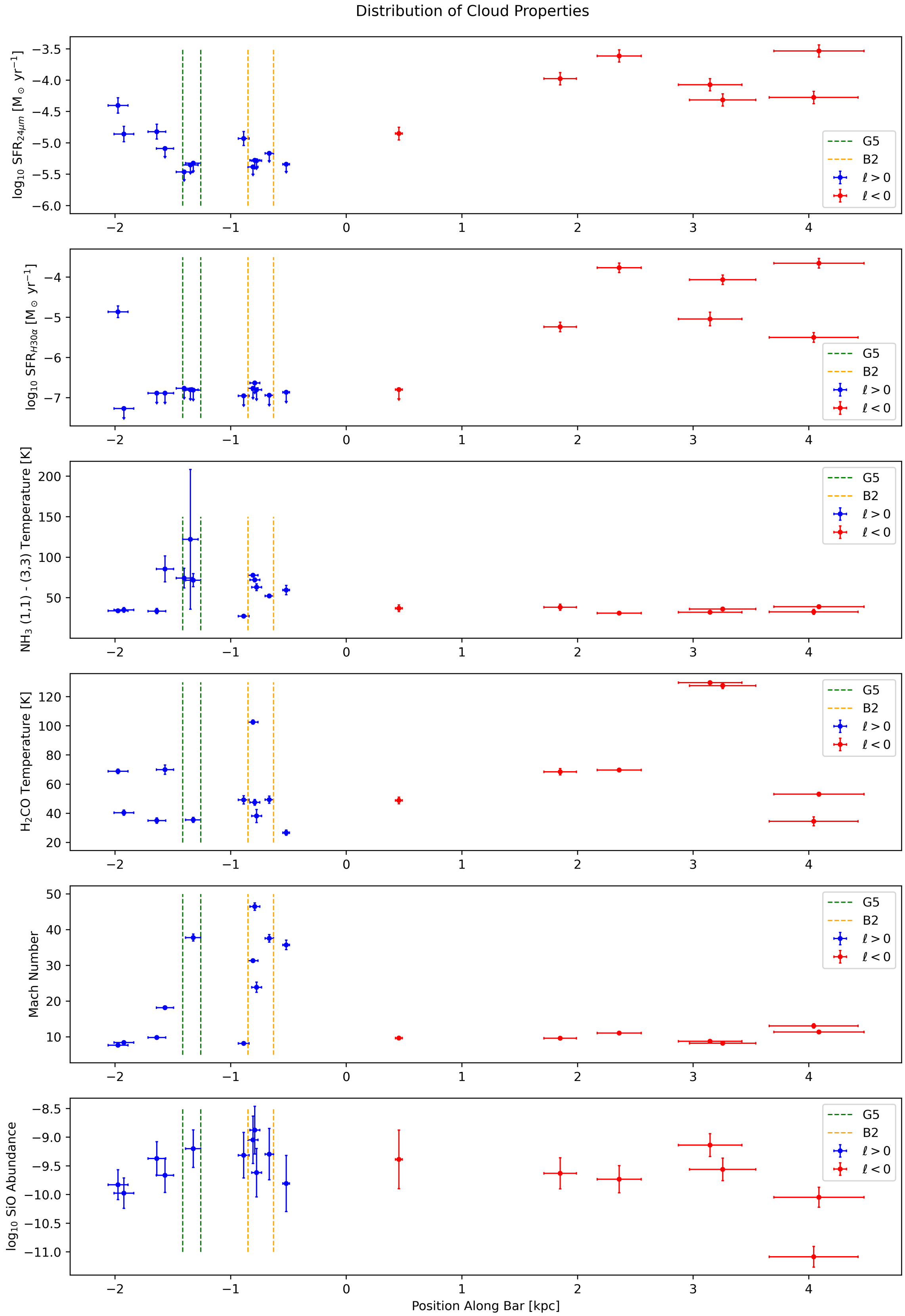

Figure 12. Distribution of properties as a function of position along the bar.

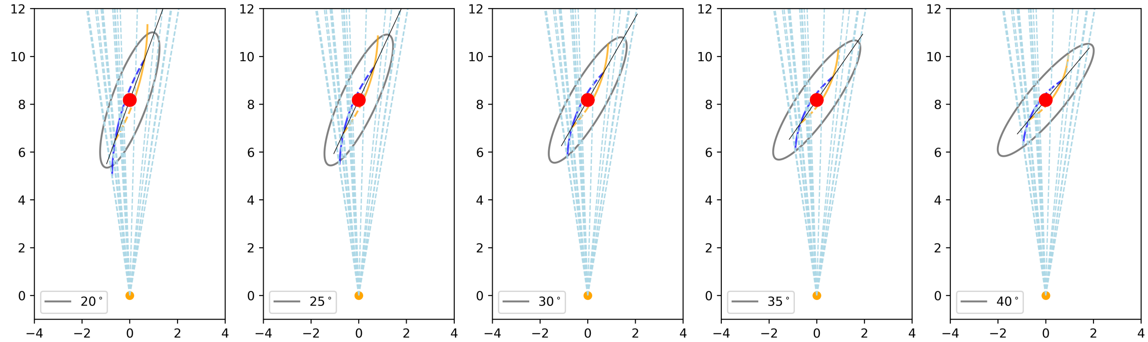

Figure 13. Geometry of bar, assuming a range of bar-sun angles from 20° to 40°. Regardless of angle, it appears that negative ℓ sources are at different Galactic locations than positive ℓ, even if they all lie on the bar.

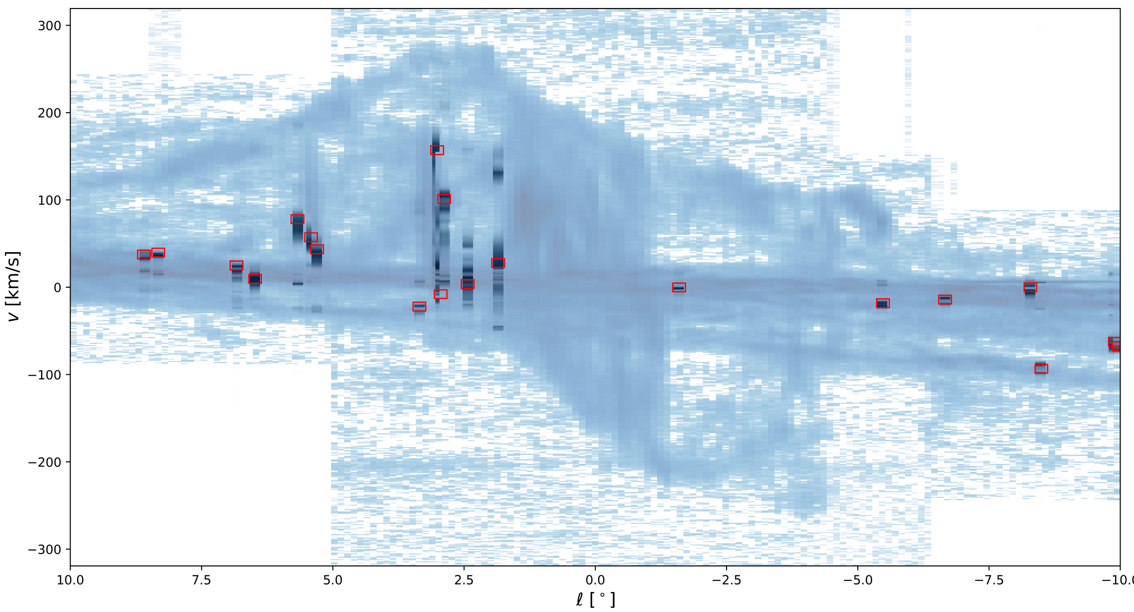

Figure 14. The longitude-velocity (ℓ-v) distribution of our cloud sample overlaid on CO $J = 1 \rightarrow 0$ emission from Bitran et al. (1997), in blue. The black vertical stripes are the velocity spectra of each of our clouds, located horizontally at the cloud's longitude. The red boxes are centered on the central velocity of each cloud.

Contopoulos, G., & Grosbøl, P. 1989, The Astronomy and Astrophysics Review, 1, 261, doi: 10.1007/BF00873080

Fazio, G. G., Hora, J. L., Allen, L. E., et al. 2004, The Astrophysical Journal Supplement Series, 154, 10, doi: 10.1086/422843

Garay, G., Mardones, D., & Rodríguez, L. F. 2000, The Astrophysical Journal, 545, 861, doi: 10.1086/317853

Ginsburg, A., Henkel, C., Ao, Y., et al. 2016, Astronomy and Astrophysics, 586, A50, doi: 10.1051/0004-6361/201526100

Ginsburg, A., Koch, E., Robitaille, T., et al. 2019, radio-astro-tools/spectral-cube: Release v0.4.5, Zenodo, doi: 10.5281/zenodo.3558614

Harris, C. R., Millman, K. J., Van Der Walt, S. J., et al. 2020, Nature, 585, 357, doi: 10.1038/s41586-020-2649-2

Hatchfield, H. P., Sormani, M. C., Tress, R. G., et al. 2021, The Astrophysical Journal, 922, 79, doi: 10.3847/1538-4357/ac1e89

Henkel, C., Mauersberger, R., Peck, A. B., Falcke, H., & Hagiwara, Y. 2000, Astronomy and Astrophysics, 361, L45, doi: 10.48550/arXiv.astro-ph/0010519

Henshaw, J. D., Longmore, S. N., Kruijssen, J. M. D., et al. 2016, Monthly Notices of the Royal Astronomical Society, 457, 2675, doi: 10.1093/mnras/stw121

Huettemeister, S., Wilson, T. L., Mauersberger, R., et al. 1995, Astronomy and Astrophysics, 294, 667. https://ui.adsabs.harvard.edu/abs/1995A&A...294..667H

Hunt, L. K., & Hirashita, H. 2009, Astronomy and Astrophysics, 507, 1327, doi: 10.1051/0004-6361/200912020

Hunter, J. D. 2007, Computing in Science & Engineering, 9, 90, doi: 10.1109/MCSE.2007.55

Jones, P. A., Burton, M. G., Cunningham, M. R., et al. 2012, Monthly Notices of the Royal Astronomical Society, 419, 2961, doi: 10.1111/j.1365-2966.2011.19941.x

Kauffmann, J., Pillai, T., Zhang, Q., et al. 2017, Astronomy & Astrophysics, 603, A89, doi: 10.1051/0004-6361/201628088

Keto, E., Zhang, Q., & Kurtz, S. 2008, The Astrophysical Journal, 672, 423, doi: 10.1086/522570

Kim, W. J., Urquhart, J. S., Wyrowski, F., Menten, K. M., & Csengeri, T. 2018, Astronomy and Astrophysics, 616, A107, doi: 10.1051/0004-6361/201732330

Kruijssen, J. M. D., Longmore, S. N., Elmegreen, B. G., et al. 2014, Monthly Notices of the Royal Astronomical Society, 440, 3370, doi: 10.1093/mnras/stu494

Krumholz, M. R., Kruijssen, J. M. D., & Crocker, R. M. 2017, Monthly Notices of the Royal Astronomical Society, 466, 1213, doi: 10.1093/mnras/stw3195

Langer, W. D., & Penzias, A. A. 1990, The Astrophysical Journal, 357, 477, doi: 10.1086/168935

Larson, R. B. 1981, Monthly Notices of the Royal Astronomical Society, 194, 809, doi: 10.1093/mnras/194.4.809

Leitherer, C., Schaerer, D., Goldader, J. D., et al. 1999, The Astrophysical Journal Supplement Series, 123, 3, doi: 10.1086/313233

Longmore, S. N., Walsh, A. J., Purcell, C. R., et al. 2017, Monthly Notices of the Royal Astronomical Society, 470, 1462, doi: 10.1093/mnras/stx1226

Lowry Manson, E., Clark, W. W., De Lucia, F. C., & Gordy, W. 1977, Physical Review A, 15, 223, doi: 10.1103/PhysRevA.15.223

Mangum, J. G., & Shirley, Y. L. 2015, Publications of the Astronomical Society of the Pacific, 127, 266, doi: 10.1086/680323

Martin-Pintado, J., Bachiller, R., & Fuente, A. 1992, Astronomy and Astrophysics, 254, 315. https://ui.adsabs.harvard.edu/abs/1992A&A...254..315M

Martins, F., Schaerer, D., & Hillier, D. J. 2005, Astronomy and Astrophysics, 436, 1049, doi: 10.1051/0004-6361:20042386

Meier, D. S., & Turner, J. L. 2005, The Astrophysical Journal, 618, 259, doi: 10.1086/426499

Mills, E. A. C., Ginsburg, A., Immer, K., et al. 2018, The Astrophysical Journal, 868, 7, doi: 10.3847/1538-4357/aae581

Mizuno, D. R., Carey, S. J., Noriega-Crespo, A., et al. 2008, Publications of the Astronomical Society of the Pacific, 120, 1028, doi: 10.1086/591809

Murphy, E. J., Condon, J. J., Schinnerer, E., et al. 2011, The Astrophysical Journal, 737, 67, doi: 10.1088/0004-637X/737/2/67

Oka, T., Geballe, T. R., Goto, M., Usuda, T., & McCall, B. J. 2005, The Astrophysical Journal, 632, 882, doi: 10.1086/432679

Ott, J., Weiss, A., Henkel, C., & Walter, F. 2005, The Astrophysical Journal, 629, 767, doi: 10.1086/431661

Perez, F., & Granger, B. E. 2007, Computing in Science & Engineering, 9, 21, doi: 10.1109/MCSE.2007.53

Povich, M. S., Stone, J. M., Churchwell, E., et al. 2007, The Astrophysical Journal, 660, 346, doi: 10.1086/513073

Purcell, C. R., Longmore, S. N., Walsh, A. J., et al. 2012, Monthly Notices of the Royal Astronomical Society, 426, 1972, doi: 10.1111/j.1365-2966.2012.21800.x

Quireza, C., Rood, R. T., Bania, T. M., Balser, D. S., & Maciel, W. J. 2006, The Astrophysical Journal, 653, 1226, doi: 10.1086/508803

Rahman, M., & Murray, N. 2010, The Astrophysical Journal, 719, 1104, doi: 10.1088/0004-637X/719/2/1104

Raymonda, J. W., Muenter, J. S., & Klemperer, W. A. 1970, Journal of Chemical Physics, 52, 3458, doi: 10.1063/1.1673510

Rieke, G. H., Young, E. T., Engelbracht, C. W., et al. 2004, The Astrophysical Journal Supplement Series, 154, 25, doi: 10.1086/422717

Rivera-Soto, R., Galván-Madrid, R., Ginsburg, A., & Kurtz, S. 2020, The Astrophysical Journal, 899, 94, doi: 10.3847/1538-4357/aba749

Schilke, P., Walmsley, C. M., Pineau des Forets, G., & Flower, D. R. 1997, Astronomy and Astrophysics, 321, 293. https://ui.adsabs.harvard.edu/abs/1997A&A...321..293S

Scoville, N., & Murchikova, L. 2013, The Astrophysical Journal, 779, 75, doi: 10.1088/0004-637X/779/1/75

Sormani, M. C., & Barnes, A. T. 2019, Monthly Notices of the Royal Astronomical Society, 484, 1213, doi: 10.1093/mnras/stz046

Sormani, M. C., Binney, J., & Magorrian, J. 2015, Monthly Notices of the Royal Astronomical Society, 449, 2421, doi: 10.1093/mnras/stv441

Sormani, M. C., Treß, R. G., Ridley, M., et al. 2018, Monthly Notices of the Royal Astronomical Society, 475, 2383, doi: 10.1093/mnras/stx3258

Sormani, M. C., Treß, R. G., Glover, S. C. O., et al. 2019, Monthly Notices of the Royal Astronomical Society, 488, 4663, doi: 10.1093/mnras/stz2054

Stark, A. A., & Bania, T. M. 1986, The Astrophysical Journal, 306, L17, doi: 10.1086/184695

Storey, P. J., & Hummer, D. G. 1995, Monthly Notices of the Royal Astronomical Society, 272, 41, doi: 10.1093/mnras/272.1.41

Syed, J., Wang, Y., Beuther, H., et al. 2020, Astronomy & Astrophysics, 642, A68, doi: 10.1051/0004-6361/202038449

Tak, F. F. S. v. d., Black, J. H., Schöier, F. L., Jansen, D. J., & Dishoeck, E. F. v. 2007, Astronomy & Astrophysics, 468, 627, doi: 10.1051/0004-6361:20066820

Tang, X. D., Henkel, C., Menten, K. M., et al. 2018, Astronomy & Astrophysics, 609, A16, doi: 10.1051/0004-6361/201731849

The Astropy Collaboration, Price-Whelan, A. M., Lim, P. L., et al. 2022, The Astrophysical Journal, 935, 167, doi: 10.3847/1538-4357/ac7c74

The CASA Team, Bean, B., Bhatnagar, S., et al. 2022, Publications of the Astronomical Society of the Pacific, 134, 114501, doi: 10.1088/1538-3873/ac9642

Tsuboi, M., Miyazaki, A., & Uehara, K. 2015, Publications of the Astronomical Society of Japan, 67, 90, doi: 10.1093/pasj/psv058

Urquhart, J. S., Hoare, M. G., Purcell, C. R., et al. 2010, Publications of the Astronomical Society of Australia, 27, 321, doi: 10.1071/AS10002

Virtanen, P., Gommers, R., Oliphant, T. E., et al. 2020, Nature Methods, 17, 261, doi: 10.1038/s41592-019-0686-2

Walsh, A. J., Breen, S. L., Britton, T., et al. 2011, Monthly Notices of the Royal Astronomical Society, 416, 1764, doi: 10.1111/j.1365-2966.2011.19115.x

Watson, C., Povich, M. S., Churchwell, E. B., et al. 2008, The Astrophysical Journal, 681, 1341, doi: 10.1086/588005

Wegg, C., Gerhard, O., & Portail, M. 2015, Monthly Notices of the Royal Astronomical Society, 450, 4050, doi: 10.1093/mnras/stv745

Wilson, T. L., & Rood, R. 1994, Annual Review of Astronomy and Astrophysics, 32, 191, doi: 10.1146/annurev.aa.32.090194.001203